Received: 29 October 2019 | Revised: 19 December 2019 | Accepted: 14 January 2020

DOI: 10.1111/jace.17034

ORIGINAL ARTICLE

Journal of the American Ceramic Society

Design of p-type NKN-based piezoelectric ceramics sintered in low oxygen partial pressure by defect engineering

Zhenxing Wang[1] | **Yu Huan**[1] | **Yue Feng**[1] | **Yu Qiu**[1] | **Tao Wei**[1] | **Ruzhong Zuo**[2]

[1]School of Material Science and Engineering, University of Jinan, Jinan, PR China

[2]Institute of Electro Ceramics & Devices, School of Materials Science and Engineering, Hefei University of Technology, Hefei, PR China

Correspondence
Yu Huan, School of Material Science and Engineering, University of Jinan, Jinan, 250022, PR China.
Email: mse_huany@ujn.edu.cn

Ruzhong Zuo, Institute of Electro Ceramics & Devices, School of Materials Science and Engineering, Hefei University of Technology, Hefei, 230009, PR China.
Email: piezolab@hfut.edu.cn

Funding information
National Natural Science Foundation of China, Grant/Award Number: 51702119, 51702122 and 51972146

Abstract

The reduction-resistant properties of piezoelectric ceramics are of great importance for multilayer monolithic structures based on base metal inner electrodes, particularly for recently reported niobate-based lead-free perovskites. In this letter, the Hall-effect measurement and impedance analysis indicate that conventional (K,Na)NbO_3 (NKN)-based ceramics exhibit an n-type electronic conduction. Rapid increase in the concentrations of oxygen vacancies and electrons is responsible for severe degradation of resistivity and piezoelectric properties as sintered in N_2. By comparison, p-type NKN-based ceramics by Mn doping exhibit excellent electrical properties ($d_{33} = 368$ pC/N, $d^*_{33} = 643$ pm/V, $\tan\delta = 0.019$, and IR = 39.9 G$\Omega \cdot$ cm) in N_2 sintering atmosphere, as well interpreted by a series of proposed defect chemistry equations. The experimental results suggest that an introduction of the p-type conduction behavior should be an effective strategy to enabling NKN-based ceramics and Cu/Ni electrodes to well co-fire in a weakly reducing atmosphere.

1 | INTRODUCTION

Pb(Zr,Ti)O_3-based solid solution ceramics occupy a predominant position in the piezoelectric electronic devices due to their excellent piezoelectric properties. However, Pb element seriously pollutes the environment and harms the human health. Therefore, many lead-free piezoelectric systems including (Na,K)NbO_3 (NKN)- and ($Bi_{0.5}Na_{0.5}$)TiO_3-based ceramics have been explored to replace Pb-based ceramics in the past decades. Since the nontextured ceramics with excellent piezoelectric performances (piezoelectric coefficient d_{33} ~ 570 pC/N) were developed, NKN-based piezoceramics attracted much attention.[1,2]

Among various device applications of piezoelectric ceramics, multilayer monolithic structures, for example, piezoelectric actuators for focusing of cameras or weaving of warp knitting machines, provide many advantages such as low driving voltage, large displacement, and so on, in which precious metals Ag/Pd are usually used as inner electrodes.[3] However, Ag elements easily diffuse into perovskite ceramic layers in service especially under high external electric fields, leading to the degradation of piezoelectric devices probably through sharply rising leakage current.[4] Besides, the increased manufacturing cost, especially from the inner electrodes, should not be welcomed. Therefore, base metal inner electrodes, such as Cu/Ni, are strongly recommended.

To prevent inner electrodes from oxidation, sintering process should be finished in low oxygen partial pressure to enable NKN-based piezoelectric multilayer structures based on Cu/Ni inner electrodes to work appropriately.[5,6] Unfortunately, it is a common fact that their piezoelectric properties would degrade seriously when NKN-based ceramics are sintered in low oxygen partial pressure.[7] The relevant mechanism was especially in this work ascribed to rapidly increased electron concentration in low oxygen partial pressure, because conventional NKN-based ceramics

exhibit an n-type conduction mechanism. A special design of p-type NKN-based ceramics by defect engineering was reported, considering the low oxygen partial pressure during sintering process can depress the generation of the holes, resulting the high resistivity. As a result, excellent electrical properties of piezoelectric coefficient d_{33} of 368 pC/N and resistivity of 39.9 GΩ · cm were obtained in the 0.3 mol% MnO-doped NKN-based lead-free ceramics sintered in N_2 sintering atmosphere.

2 | EXPERIMENTAL PROCEDURE

$0.95(Na_{0.5}K_{0.5})NbO_3$-$0.05(Bi_{0.5}Na_{0.5})ZrO_3$ (abbreviated to Mn0-A/Mn0-N) and $0.95(Na_{0.5}K_{0.5})NbO_3$-$0.05(Bi_{0.5}Na_{0.5})ZrO_3$-0.3 mol% MnO (abbreviated to Mn-A/Mn-N) ceramics were prepared using a conventional solid-state reaction method. A or N means that the ceramics were sintered in air or N_2, respectively. The ceramics were sintered at 1090-1120°C for 2 hours. The carrier type was investigated by a Hall-effect measurement system as follows. The sample was exposed to a magnetic field and a fixed current of 10 nA was applied through a digital multimeter (2700 Multimeter acquisition system, Keithley). The Hall voltage was detected by the digital multimeter (2400 Source Meter, Keithley). Impedance spectrum over frequencies from 40 Hz to 1 MHz under a V_{rms} of 100 mV AC signal was measured by an impedance analyzer (Agilent 4294A, Agilent). Further details about experimental methods can be found in Supplementary Materials.

3 | RESULTS AND DISCUSSION

Defect structure of undoped NKN-based samples is shown in Figure 1. The carrier type and concentration are directly determined using a Hall-effect measurement as sketched in Figure 1A and Figure S1.[8] The variation of Hall voltage (V_H) with respect to applied magnetic field is plotted in Figure 1B and the measurement parameters are summarized in Table S1. The dominant charge carriers of Mn0 ceramics are electrons. The carrier concentration (c) can be calculated by the following expression:

$$c = 1/\left(e \times \frac{V_H d}{IB}\right) \quad (1)$$

where B, I, e, and d represent magnetic field, current, electronic charge, and thickness of the bulk ceramic, respectively. The electron concentration of Mn0-A is 5.21×10^7 cm^{-3}, which is smaller than that of Mn0-N (9.77×10^7 cm^{-3}).

The oxygen ions in the lattice would turn into oxygen gas, accompanied by the formation of an ionized oxygen vacancy ($V_O^{\bullet\bullet}$) and two electrons (e') when the perovskite-type piezoelectric ceramics are sintered at high temperature. The reaction can be given by:

$$O_O^{\times} \leftrightarrow 1/2O_2 \uparrow + V_O^{\bullet\bullet} + 2e' \quad (2)$$

In the meantime, the alkali metal can volatilize during sintering process, accompanied by the loss of their associated

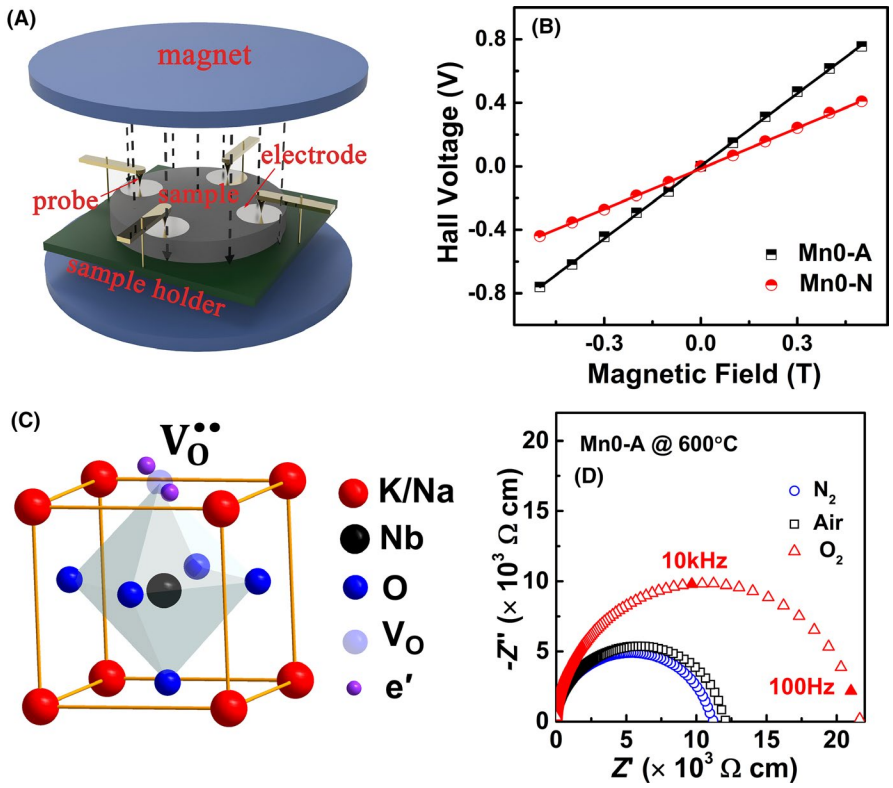

FIGURE 1 Defect structure of Mn0 ceramics: A, schematic diagram of Hall-effect measurement; B, hall voltage as a function of applied magnetic field; C, schematic illustration of defect structure for Mn0 ceramics; D, Impedance spectra of Mn0-A sample at 600°C measured in different atmospheres [Color figure can be viewed at wileyonlinelibrary.com]

suboxides. The volatilization process of alkali metal can be expressed as following equations[7,9,10]

$$2A_A^{\times} + 1/2O_2 \leftrightarrow A_2O\uparrow + 2V_A' + 2h^{\bullet} \quad (3)$$

The low oxygen partial pressure minimizes the volatilization of the alkali suboxide, leading to suppress the formation of intrinsic alkali vacancies and holes.[11] Therefore, the dominant defect structure of Mn0 ceramics is oxygen vacancies and free electrons as sketched in Figure 1C. When the Mn0 ceramics are exposed in the low oxygen partial pressure, the reaction equilibrium of Equation (2) shifts toward right hand, resulting in the rapidly raising concentrations of electron and oxygen vacancy. As the mobility of charged oxygen vacancies is notably weaker than electron carriers,[12] the change in resistivity should be mainly attributed to the change of the electron concentration.

To get a better insight into the influence of defect structure on electrical properties, impendence spectroscopy was performed on Mn0-A samples under different atmospheres including pure nitrogen ($PO_2 \sim 10^{-5}$ atm), air ($PO_2 \sim 0.2$ atm), and pure oxygen ($PO_2 \sim 1$ atm), as displayed in Figure 1D. There is no clear evidence for the presence of a spike or arc associated with Warburg diffusion and oxygen ion conduction at low frequency down to 40 Hz as observed from the Nyquist plots, which means that electron charges are primarily responsible for the conductivity response.[13,14] In addition, Z^* semicircle in N_2 exhibits a relatively small radius compared with that in O_2 and air, indicating that the resistance of Mn0-A ceramics gradually decreases with reducing oxygen partial pressure of ambient.[15]

The electron concentration of Mn0-A and Mn0-N ceramics is quantitatively analyzed by impedance spectra in Figure 2. The Nyquist plots were fitted with the assumed equivalent circuits to evaluate the equivalent R (resistance) and C (capacitance) component values.[16,17] Only one broad peak in Z'' spectra in Figure 2C and Figure S2A confirms one RC element in the assumed equivalent circuit. All the complex plane plots are slightly depressed instead of being centered on the abscissa axis.[18] Thus, a constant phase element, CPE, replaces the standard capacitance C element to provide a better fitting result.[19] Accordingly, an equivalent electrical circuit comprising of R_b and CPE_b in Figure 2D is proposed. An excellent agreement between

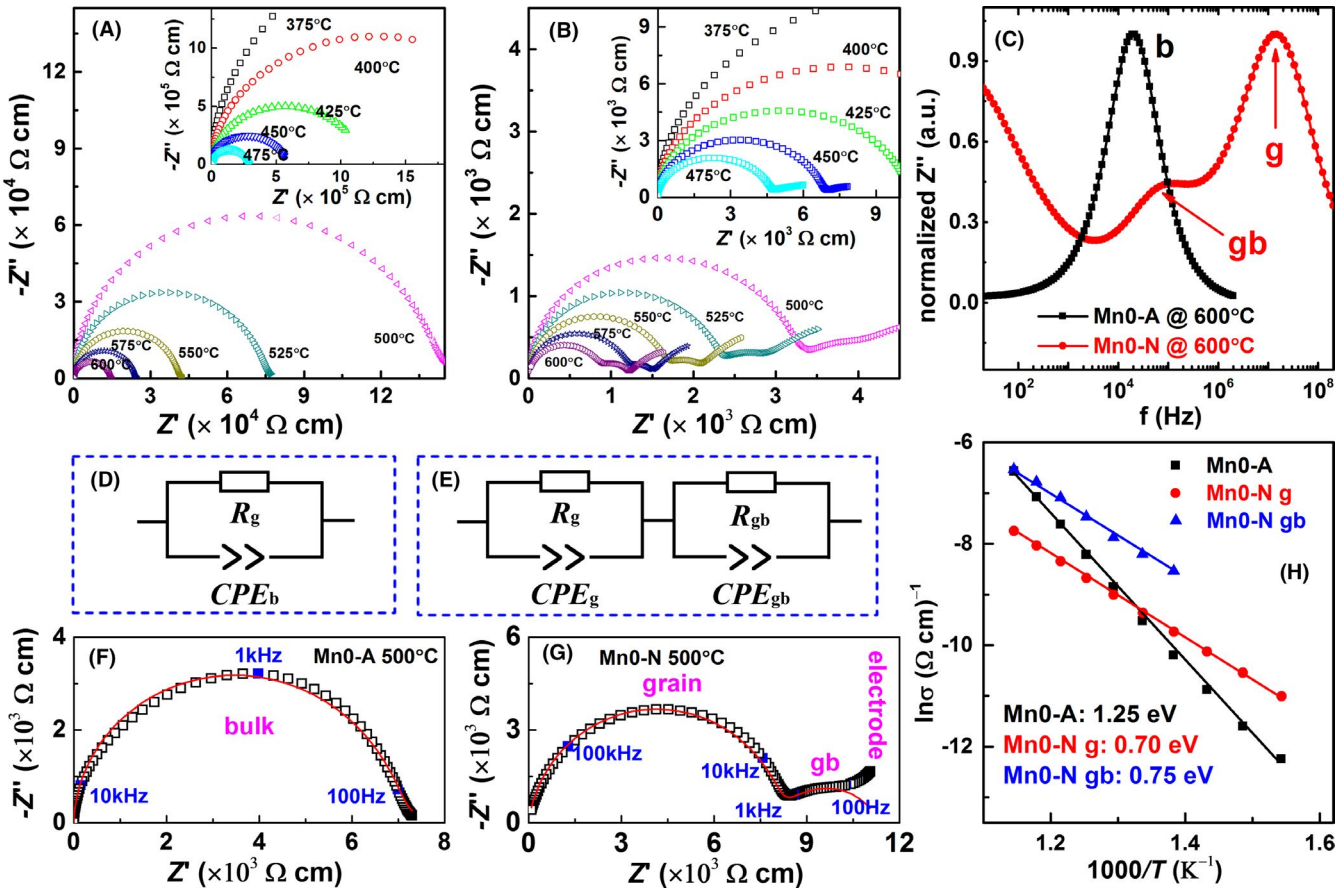

FIGURE 2 Impedance spectra of A Mn0-A and B Mn0-N; C, Z'' spectroscopic plots of Mn0-A and Mn0-N samples at 600°C; the proposed electrical equivalent circuit for (D) Mn0-A and (E) Mn0-N; experimental (black scatter) and fitting curves (red continuous line) of the impedance spectrum for (F) Mn0-A and (G) Mn0-N at 500°C; (H) Arrhenius plots of conductivity vs 1000/T [Color figure can be viewed at wileyonlinelibrary.com]

the experimental and fitting curves for Mn0-A ceramics in Figure 2F confirms that the proposed electrical equivalent circuit is reliable.

The extracted capacitance values are about 10^{-9} F in Figure S3A, which are of the same order of magnitude as typical capacitances associated with ferroelectric materials.[20] Conductivity (σ) is calculated by the extracted R_b and plotted in Figure 2H. It can be found that σ decreases by orders of magnitude with decreasing temperature, declaring the conduction behavior is a process caused by thermally activated charge carriers.[21] $\ln\sigma$ shows a linearly associated with T^{-1}, demonstrating that the conductivity is commonly governed by the Arrhenius law, which can be expressed as the following equation.

$$\sigma = \sigma_0 \exp\left(-E_{con}/k_B T\right) \quad (4)$$

where σ_0 is the high-temperature limit of the conductivity, k_B is the Boltzmann constant, and T is the temperature in Kelvin scale. The activation energy for conduction (E_{con}) of Mn0-A is calculated as ~1.25 eV, which is associated with electrons derived from $V_O^{\bullet\bullet}$ with respect to References [22,23].

Impedance plane plots of Mn0-N are much different from those of Mn0-A sample as shown in Figure 2B. Mn0-N samples look electrically heterogeneous, where the high-frequency and intermediate-frequency arcs are assigned to the grain and grain boundary responses, respectively.[27] The incomplete semicircle at low frequency is associated with ceramic-electrode interaction contribution (Supplementary Materials). In addition, a main peak and a shoulder are present in Z'' spectroscopic plots (Figure 2C and Figure S2B). Therefore, two *R-CPE* elements superimposed on each other are proposed to model the experimental impedance data, as sketched in Figure 2E, where *g* and *gb* stand for grain and grain boundary, respectively. The experimental data coincide well with the simulated curve fitted in Figure 2G.

The extracted capacitances related to the high-frequency and intermediate-frequency semicircles are ~10^{-9} and 10^{-7} F in Figures S3B–C, which are typical capacitances associated with grain and grain boundary responses, respectively.[20,28] The conductivity calculated by the extracted resistance is plotted in Figure 2H. The resistivity of Mn0-N is much smaller than that of Mn0-A at the same measuring temperature, indicating the higher electron concentration

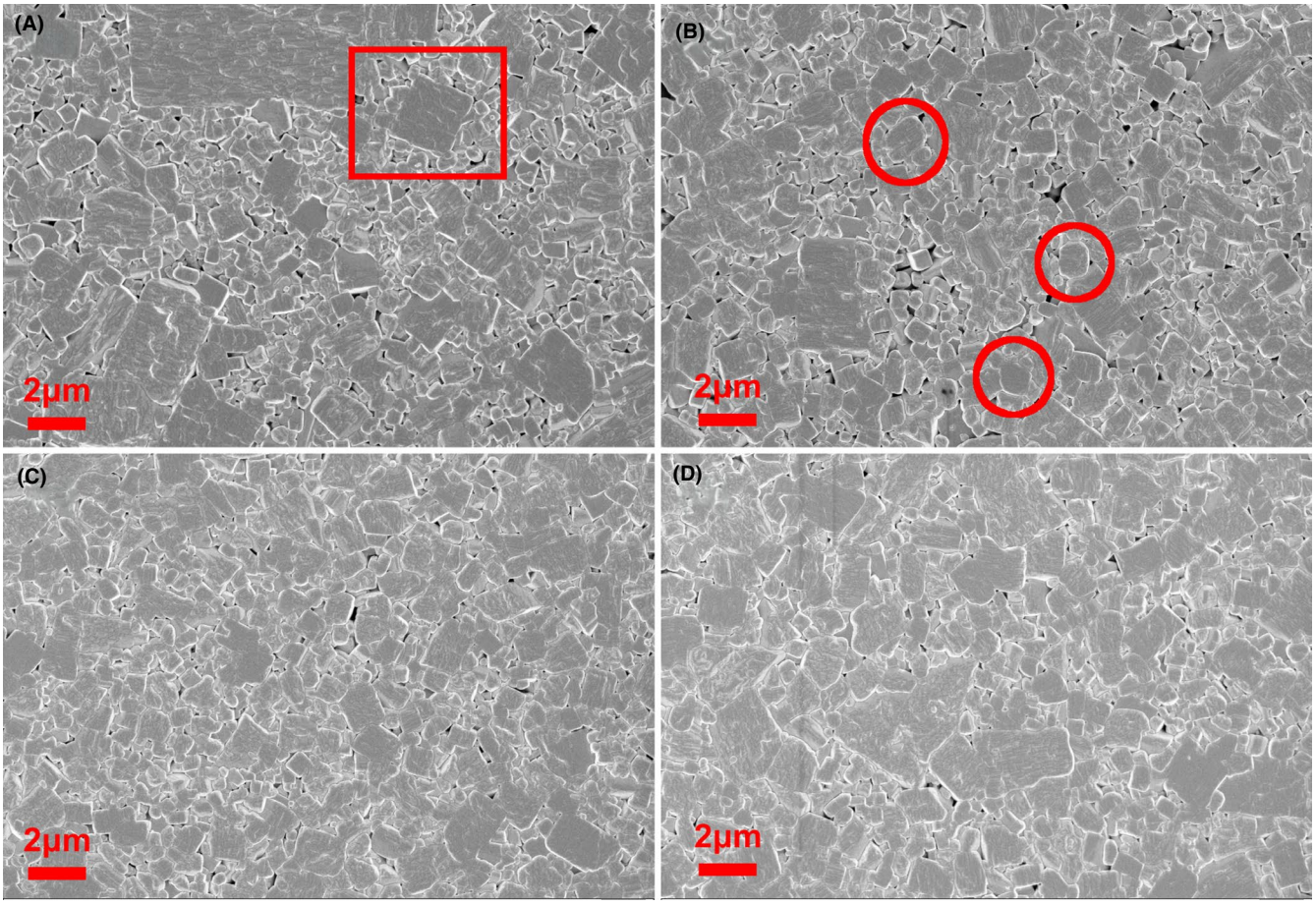

FIGURE 3 SEM images of (A) Mn0-A, (B) Mn0-N, (C) Mn-A, and (D) Mn-N ceramics [Color figure can be viewed at wileyonlinelibrary.com]

TABLE 1 Electrical properties of the NKN-based ceramics sintered in different atmospheres

Sample	d_{33} (pC/N)	d^*_{33} (pm/V)	k_p (%)	ε^T_{33}	tanδ	IR (G$\Omega \cdot$ cm)	Relative density (%)
Mn0-A	304	561	0.336	1704	0.025	33.6	95.3
Mn0-N	257	451	0.292	1395	0.056	8.8	94.3
Mn-A	359	605	0.404	1967	0.021	39.3	97.6
Mn-N	368	643	0.428	1978	0.019	39.9	97.9

in Mn0-N in accordance with the Hall-effect measurement. The activation energies calculated by the Arrhenius law from grain and grain boundary contribution are 0.70 and 0.75 eV, respectively, which demonstrates that the conduction mechanism is predominately controlled by electrons.[25,26,29] The activation energy value of Mn0-N is much smaller than that of Mn0-A ceramics. Considering E_{con} is the migration free energy of charge carriers over a long distance,[21] the electrons in Mn0-N ceramics have higher migration rate.

The XRD patterns of Mn0-A and Mn0-N ceramics are shown in Figure S5. The site occupancies, lattice parameters, cell volumes, and refinement parameters are summarized in Tables S2 and S3. The lattice lengths of Mn0-N are a little smaller than that of Mn0-A samples, which should be ascribed to the higher oxygen vacancy concentration in Mn0-N ceramics. A significant different microscopic morphology is observed between the Mn0 ceramics sintered in air and N_2 atmosphere as displayed in Figure 3A,B. Observed from the SEM images, Mn0-A ceramics exhibit cubic or rectangular grains with a clear and well-defined grain boundary marked with the red squares. Whereas the grain morphology becomes round-shaped (marked with the red circles) for Mn0-N, indicating the high defect concentration based on the two-dimensional nucleation-controlled theory.[5,7] Besides, it is found that the grain growth of the NKN-based ceramics is slightly supressed in low oxygen partial pressure, which is similar with some previous reports.[5] The compactness of Mn0-N sample is obviously lower than that of Mn0-A ceramic, which is in consistent with the relative density measured by Archimedes method as summarized in Table 1.

Figure 4A–D illustrate *P–E* hysteresis loops and unipolar *S–E* curves measured at 1 Hz of the undoped NKN-based ceramics sintered in air and N_2. The piezoelectric properties, normalized strain (d^*_{33}) at 1 kV/mm, dielectric properties and insulation resistivity (IR) are summarized in Table 1. The coercive electric field (E_c) of Mn0-N (~1.25 kV/mm) is larger than that of Mn0-A (~1.13 kV/mm). Additionally, the dielectric loss tanδ and IR degrade severely when the Mn0 ceramics are sintered in N_2, indicating the high defect concentration

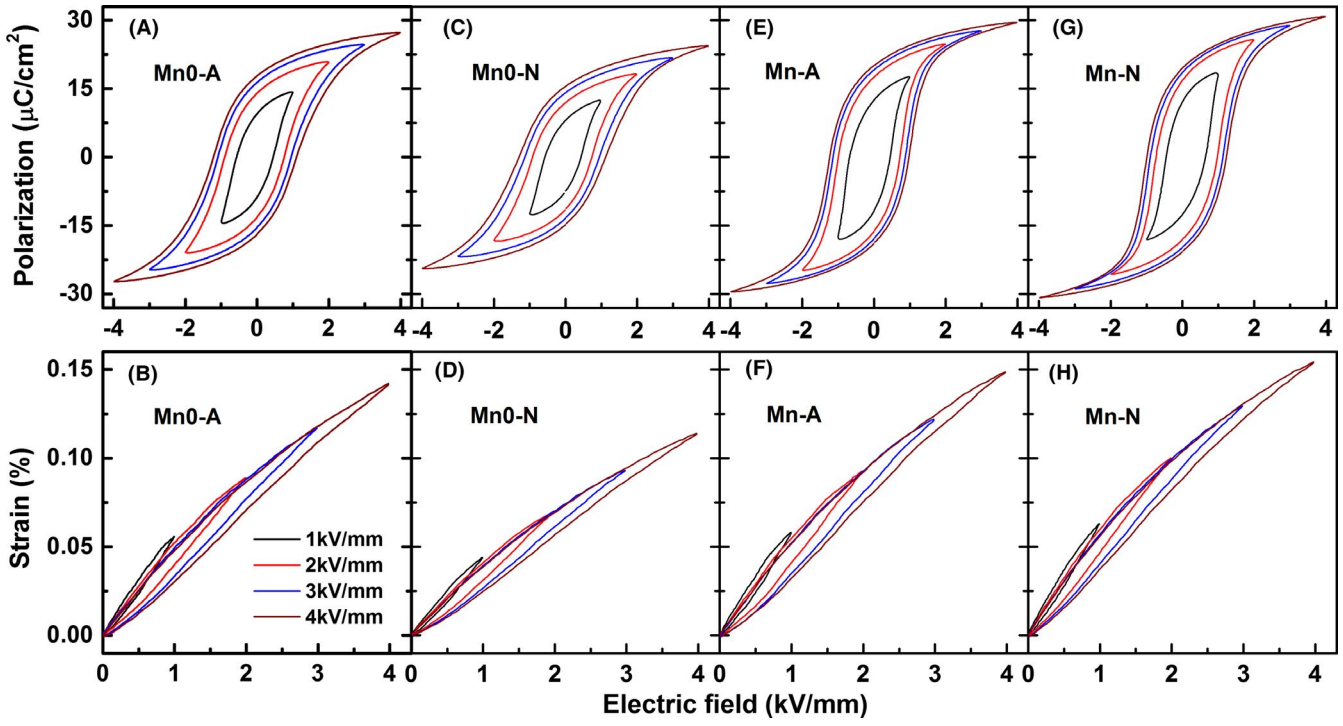

FIGURE 4 *P–E* hysteresis loops of (A) Mn0-A, (C) Mn0-N, (E) Mn-A, and (G) Mn-N ceramics; Unipolar *S–E* strain curves of (B) Mn0-A, (D) Mn0-N, (F) Mn-A, and (H) Mn-N ceramics [Color figure can be viewed at wileyonlinelibrary.com]

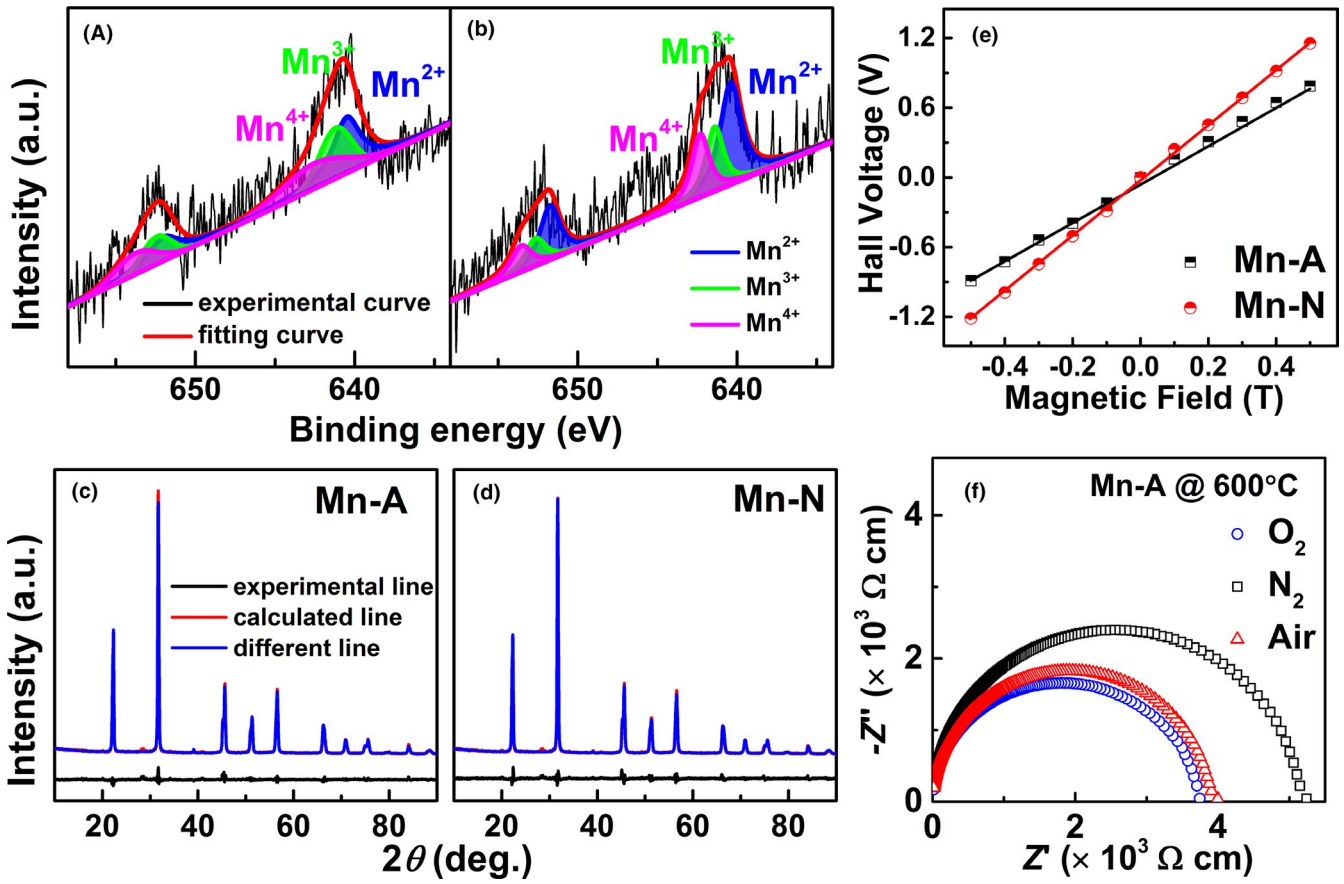

FIGURE 5 Defect structure of Mn-doped ceramics: XPS of Mn 2p for (A) Mn-A and (B) Mn-N samples; Rietveld refinement XRD patterns of (C) Mn-A and (D) Mn-N ceramics; (E) Hall voltage as a function of applied magnetic field; (F) Impedance spectra of Mn-A sample at 600°C measured in different atmosphere [Color figure can be viewed at wileyonlinelibrary.com]

in Mn0-N ceramics. These defects will pinch the domain wall motions, resulting in the low saturated polarization and remnant polarization of the Mn0-N ceramics as displayed in Figure 4C. Accordingly, the dielectric property (ε_{33}^{T}) and piezoelectric properties (including d_{33}, d_{33}^{*}, and k_p) degrade seriously for Mn0-N ceramics. To sum up, the electron concentration increases rapidly when the undoped NKN-based ceramics with an n-type conduction mechanism are sintered in low oxygen partial pressure, which is responsible for the severely degraded electrical properties.

To explore the defect structure of Mn-doped NKN-based ceramics, the valence states of elements are checked by XPS analysis in Figure S6 and Figure 5A,B. The Mn 2p XPS spectra are fitted by Gaussian-Lorenz function and content of Mn elements in different valance state are listed in Table S4. The fitting results and asymmetrical XPS spectra confirm the multiple Mn valance states.[30] The crystal structure of Mn-doped ceramics is investigated by Rietveld refinement in Figure 5C,D. The site occupancies, lattice parameters, cell volumes, and refinement parameters are summarized in Tables S5 and S6. The refinement results demonstrate that the Mn ions prefer to substitute B site. XPS analysis in Figure S6 indicates that multiple Mn valance states including Mn^{2+}, Mn^{3+}, and Mn^{4+}, exist in the ceramics. In addition, the content of Mn^{2+} is lower than the combined content of Mn^{3+} and Mn^{4+}. The ionic radius of Mn^{2+} with 6 CN is larger than that of B-site ions (Nb^{5+} and Zr^{4+}), while the ionic radius

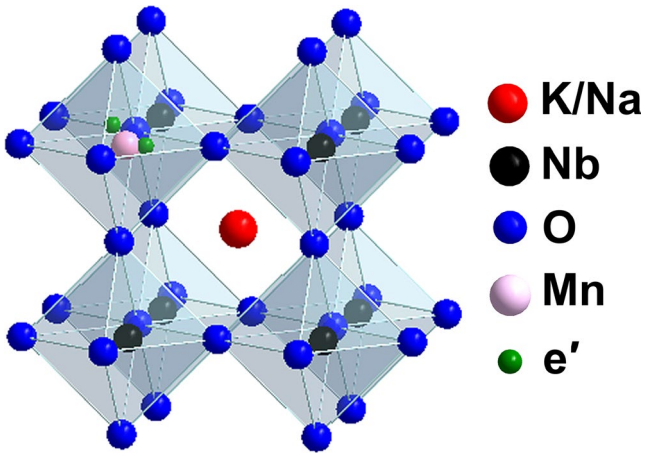

FIGURE 6 Schematic illustration of defect structure for Mn-doped ceramics [Color figure can be viewed at wileyonlinelibrary.com]

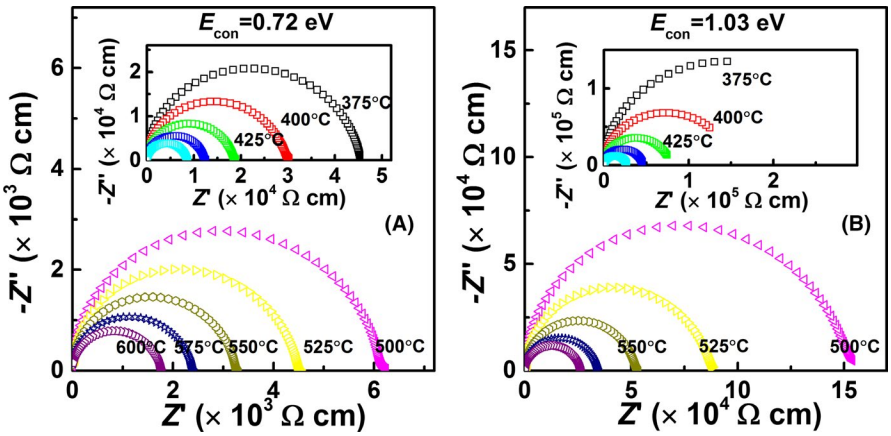

FIGURE 7 Impedance spectra of (A) Mn-A and (B) Mn-N [Color figure can be viewed at wileyonlinelibrary.com]

of Mn^{3+}/Mn^{4+} with 6 CN is smaller than that of B-site ions as shown in Table S7. Therefore, the lattice parameters of Mn-doped ceramics are smaller than that of pure NKN-based ceramics. The incorporation reactions of Mn ions into ABO_3 lattices are expressed by the following equations:

$$2MnO \longrightarrow Nb_2O_5 2Mn'''_{Nb} + 2O^{\times}_{O} + 3V^{\bullet\bullet}_{O} \quad (5)$$

$$2MnO \longrightarrow Nb_2O_5 2Mn''_{Nb} + 2O^{\times}_{O} + 3V^{\bullet\bullet}_{O} + 2e' \quad (6)$$

$$2MnO \longrightarrow Nb_2O_5 2Mn'_{Nb} + 2O^{\times}_{O} + 3V^{\bullet\bullet}_{O} + 4e' \quad (7)$$

The generated $V^{\bullet\bullet}_{O}$ can promote the reaction equilibrium of Equation (2) to shift toward left hand, suppressing the volatilization of oxygen ions. It can be inferred that ionic defects of Mn'''_{Nb}, Mn''_{Nb}, and Mn'_{Nb} are dominating defects as sketched in Figure 6. These negatively charged ionic defects would capture positively charged holes. Hence Equation (8) occurs in the p-type NKN-based ceramics.

$$O^{\times}_{O} + 2h^{\bullet} \leftrightarrow V^{\bullet\bullet}_{O} + 1/2O_2 \uparrow \quad (8)$$

The reaction equilibrium shifts toward right hand in the low oxygen partial pressure, resulting in the decreasing hole concentration in the ceramics.

The dominant charge carriers of Mn-doped ceramics are holes, which were verified by Hall-effect measurement in Figure 5E. And the hole concentration decreases accompanied by the increasing Hall resistivity when the Mn-doped ceramics are sintered in N_2 as shown in Table S1. Z^* semicircle in O_2 exhibits a smaller radius than that in N_2 and air, indicating that the resistance of the Mn-doped ceramics decreases with increasing oxygen partial pressure of ambient as observed from Figure 5F. Therefore, the free holes are predominantly responsible for the conductivity response in Mn-doped ceramics.

The hole concentration of Mn-doped ceramics sintered in air and N_2 is quantitatively evaluated using the impedance spectroscopy in Figure 7. The Nyquist plots of Mn-doped ceramics are fitted with the equivalent equivalent circuits in Figure 2D. The extracted conductivity σ of Mn-doped samples is plotted in Figure S10. It is noted that the resistivity of Mn-N is larger than that of Mn-A ceramics, which is an indication of the lower hole concentration in Mn-N ceramics. And E_{con} of Mn-N (~1.03 eV) is larger than that of Mn-A (~0.72 eV), which means the higher hole mobility in Mn-A ceramic.

Low hole concentration and mobility in the Mn-N sample have a positive influence on electrical properties, such as the higher resistivity, lower dielectric loss, and smaller coercive electric field in Figure 4E,H and Table 1. It also enhances the poling efficiency as verified by the larger spontaneous and remnant polarization as observed from *P–E* hysteresis loops. Accordingly, better piezoelectric properties (including d_{33}, d^*_{33}, and k_p) and dielectric property (ε^T_{33}) are obtained in the Mn-N sample. The microscopic morphology of Mn-doped ceramics is shown in Figure 3C,D. It can be found that the ceramics sintered in N_2 and air exhibit a similar microstructure. In addition, the relative density of Mn-N and Mn-A ceramics are comparatively high, which are both higher than that of undoped ceramics as shown in Table 1. The high compactness of Mn-doped ceramics is beneficial to enhance their electrical properties.

4 | CONCLUSIONS

In summary, the correlation between defect configuration, sintering atmosphere, and electrical properties for NKN-based lead-free ceramics was systematically investigated in this work. Conventional NKN-based ceramics are proved to exhibit an n-type electronic conduction mechanism based on the impedance analysis and Hall-effect measurement. The electron concentration would increase rapidly when the ceramics are sintered in N_2, inducing the severe degradation of

resistivity and piezoelectric properties. To sinter the ceramics in low oxygen partial pressure, p-type NKN-based ceramics by doping 0.3 mol% MnO are designed under the guidance of defect chemistry theory. The experimental results confirm that the low oxygen partial pressure can depress the generation of holes during sintering process, resulting the high resistivity and excellent electrical properties ($d_{33} = 368$ pC/N, $d^*_{33} = 643$ pm/V, and IR = 39.9 GΩ · cm). This work demonstrates that designing p-type ceramics would be a rational strategy to manufacturing the NKN-based piezoelectric multilayer monolithic devices based on Cu/Ni inner electrodes.

ACKNOWLEDGMENTS

The work was supported by National Natural Science Foundation of China (Grant Nos. 51702119, 51702122, 51972146).

ORCID

Yu Huan https://orcid.org/0000-0002-6508-0801
Ruzhong Zuo https://orcid.org/0000-0001-8295-4323

REFERENCES

1. Xu K, Li J, Lv X, Wu JG, Zhang XX, Xiao DQ, et al. Superior piezoelectric properties in potassium–sodium niobate lead-free ceramics. Adv. Mater. 2016;28:8519–23.
2. Liu Q, Zhang Y, Gao J, Zhou Z, Wang H, Wang K, et al. High-performance lead-free piezoelectrics with local structural heterogeneity. Energy Environ. Sci. 2019;11:3531–9.
3. Zuo R, Li L, Gui Z, Hu X, Ji C. Effects of additives on the interfacial microstructure of cofired electrode-ceramic multilayer systems. J. Am. Ceram. Soc. 2002;85:787–93.
4. Gao RL, Chu XC, Huan Y, Zhong ZJ, Wang XH, Li LT. Ceramic–electrode inter-diffusion of (K, Na)NbO_3-based multilayer ceramics with $Ag_{0.7}Pd_{0.3}$ electrode. J. Eur. Ceram. Soc. 2015;35:389–92.
5. Fisher JG, Kang S-JL. Microstructural changes in $(K_{0.5}Na_{0.5})NbO_3$ ceramics sintered in various atmospheres. J. Eur. Ceram. Soc. 2009;29:2581–8.
6. Gao LS, Ko SW, Guo HZ, Hennig E, Randall CA. Demonstration of copper co-fired (Na, K)Nb_O3 multilayer structures for piezoelectric applications. J. Am. Ceram. Soc. 2016;99:2017–23.
7. Huan Y, Wang X, Wei T, Xie J, Ye Z, Zhao P, et al. Defect engineering of high-performance potassium sodium niobate piezoelectric ceramics sintered in reducing atmosphere. J. Am. Ceram. Soc. 2017;100:2024–33.
8. Bae S-H, Kahya O, Sharma BK, Kwon J, Cho HJ, Özyilmaz B, et al. Graphene-P(VDF-TrFE) multilayer film for flexible applications. ACS Nano. 2013;7:3130–8.
9. Huan Y, Wang X, Wei T, Zhao P, Xie J, Ye Z, et al. Defect control for enhanced piezoelectric properties in SnO_2 and ZrO_2 co-modified KNN ceramics fired under reducing atmosphere. J. Eur. Ceram. Soc. 2017;37:2057–65.
10. Gong HL, Wang XH, Zhang SP, Tian ZB, Li LT. Electrical and reliability characteristics of Mn-doped nano $BaTiO_3$-based ceramics for ultrathin multilayer ceramic capacitor application. J. Appl. Phys. 2012;112:114119.
11. Kobayashi K, Doshida Y, Mizuno Y, Randall CA. A route forwards to narrow the performance gap between PZT and lead-free piezoelectric ceramic with low oxygen partial pressure processed $(Na_{0.5}K_{0.5})NbO_3$. J. Am. Ceram. Soc. 2012;95:2928–33.
12. Kumar N, Patterson EA, Froemling T, Cann DP. Conduction mechanisms in $BaTiO_3$-$Bi(Zn_{1/2}Ti_{1/2})O_3$ ceramics. J. Am. Ceram. Soc. 2016;99:3047–54.
13. Li M, Pietrowski MJ, De Souza RA, Zhang H, Reaney IM, Cook SN, et al. A family of oxide ion conductors based on the ferroelectric perovskite $Na_{0.5}Bi_{0.5}TiO_3$. Nat. Mater. 2014;13:31–5.
14. Donnelly NJ, Randall CA. Mixed conduction and chemical diffusion in a $Pb(Zr_{0.53}Ti_{0.47})O_3$ buried capacitor structure. Appl. Phys. Lett. 2010;96:052906.
15. Li M, Li L, Zang J, Sinclair DC. Donor-doping and reduced leakage current in Nb-doped $Na_{0.5}Bi_{0.5}TiO_3$. Appl. Phys. Lett. 2015;106:102904.
16. Rafiq MA, Costa ME, Tkach A, Vilarinho PM. Impedance analysis and conduction mechanisms of lead free potassium sodium niobate (KNN) single crystals and polycrystals: A comparison study. Cryst. Growth Des. 2015;15:1289–94.
17. Jamnik J, Maier J. Treatment of the impedance of mixed conductors-equivalent circuit model and explicit approximate solutions. J. Electrochem. Soc. 1999;146:4183–8.
18. Nobre MAL, Lanfredi S. Ferroelectric state analysis in grain boundary of $Na_{0.85}Li_{0.15}NbO_3$ ceramic. J. Appl. Phys. 2003;93:5557–62.
19. Gong HL, Wang XH, Zhang SP, Wen H, Li LT. Grain size effect on electrical and reliability characteristics of modified fine-grained $BaTiO_3$ ceramics for MLCCs. J. Eur. Ceram. Soc. 2014;34:1733–9.
20. Irvine JT, Sinclair DC, West AR. Electroceramics: characterization by impedance spectroscopy. Adv. Mater. 1990;2:132–8.
21. Molak A, Ksepko E, Gruszka I, Ratuszna A, Paluch M, Ujma Z. Electric permittivity and conductivity of $(Na_{0.5}Pb_{0.5})(Mn_{0.5}Nb_{0.5})O_3$ ceramics. Solid State Ionics. 2005;176:1439–47.
22. Bidault O, Goux P, Kchikech M, Belkaoumi M, Maglione M. Space-charge relaxation in perovskites. Phys. Rev. B. 1994;49:7868–73.
23. Hu BB, Zhu MK, Guo JJ, Wang Y, Zheng MP, Hou YD. Origin of relaxor behavior in $K_{1/2}Bi_{1/2}TiO_3$-$Bi(Mg_{1/2}Ti_{1/2})O_3$ investigated by electrical impedance spectroscopy. J. Am. Ceram. Soc. 2016;99:1637–44.
24. Waser R. Bulk conductivity and defect chemistry of acceptor-doped strontium titanate in the quenched state. J. Am. Ceram. Soc. 1991;74:1934–40.
25. Xu Q, Lanagan MT, Luo W, Zhang L, Xie J, Hao H, et al. Electrical properties and relaxation behavior of $Bi_{0.5}Na_{0.5}TiO_3$-$BaTiO_3$ ceramics modified with $NaNbO_3$. J. Eur. Ceram. Soc. 2016;36:2469–77.
26. Andrejs L, Fleig J. Resistance degradation in donor-doped PZT ceramic stacks with Ag/Pd electrodes: I. Phenomenology of processes. J. Eur. Ceram. Soc. 2013;33:779–94.
27. Guo X. Peculiar size effect in nanocrystalline $BaTiO_3$. Acta Mater. 2013;61:1748–56.
28. Zang J, Li M, Sinclair DC, Frömling T, Jo W, Rödel J. Impedance spectroscopy of $(Bi_{1/2}Na_{1/2})TiO_3$–$BaTiO_3$ based high-temperature dielectrics. J. Am. Ceram. Soc. 2014;97:2825–31.
29. Chu DP, McGregor BM, Migliorato P, Durkan C, Welland ME, Hasegawa K, et al. Temperature dependence of the ohmic conductivity and activation energy of $Pb_{1+y}(Zr_{0.3}Ti_{0.7})O_3$ thin films. Appl. Phys. Lett. 2001;79:518–20.

30. Cui B, Song C, Wang GY, Yan YN, Peng JJ, Miao JH, et al. Reversible ferromagnetic phase transition in electrode-gated manganites. Adv. Funct. Mater. 2014;24:7233–40.

SUPPORTING INFORMATION

Additional supporting information may be found online in the Supporting Information section.

How to cite this article: Wang Z, Huan Y, Feng Y, Qiu Y, Wei T, Zuo R. Design of p-type NKN-based piezoelectric ceramics sintered in low oxygen partial pressure by defect engineering. *J Am Ceram Soc*. 2020;103:3667–3675. https://doi.org/10.1111/jace.17034